Journal of Structural Geology 32 (2010) 1158–1169

Contents lists available at ScienceDirect

Journal of Structural Geology

journal homepage: www.elsevier.com/locate/jsg

Micromechanics of brittle faulting and cataclastic flow in Tavel limestone

Veronika Vajdova*, Wei Zhu, Tzu-Mo Natalie Chen, Teng-fong Wong

Department of Geosciences, Stony Brook University, Stony Brook, NY 11794-2100, USA

ARTICLE INFO

Article history:
Received 23 June 2009
Received in revised form
29 June 2010
Accepted 26 July 2010
Available online 3 August 2010

Keywords:
Micromechanics
Limestone
Pore collapse
Shear failure
Microstructure
Experimental

ABSTRACT

Previous studies reveal that while compact carbonate rocks display exclusively dilatancy under compressive deformation, compaction may be observed in their more porous counterparts. In their compactive behavior the porous carbonate rocks are more akin to e.g., sandstone. Whereas the micromechanics of brittle faulting and cataclastic flow in sandstone has been studied extensively, little is known about these processes in a porous limestone. To investigate both failure modes we deformed samples of Tavel limestone with porosity 10–14% to various stages of deformation in conventional triaxial configuration at confining pressures corresponding to brittle faulting and cataclastic flow and described the microstructures associated with the damage evolution using optical and electron microscopy. In this porous micritic limestone cataclasis is the dominant mechanism of deformation. The microcracks initiate as pore-emanated and while all pores contribute to microcrack initiation, it is the large pores that drive crack propagation and coalescence leading to failure. In brittle faulting, dilatancy arises from microcracks growing parallel to maximum principal stress, with their coalescence leading to shear localization. In cataclastic flow microcracks do not have preferred orientation. Interplay between pore collapse and formation of new microcracks determines the compactive versus dilatant character of the cataclastic flow.

1. Introduction

Brittle-ductile transition in rocks is associated with a broad spectrum of deformation mechanisms and failure modes that depend on extrinsic variables such as confining and pore pressures, temperature, strain rate, and pore fluid chemistry and intrinsic variables such as modal composition, grain size, and porosity (Paterson and Wong, 2005). In field settings this leads to complex deformation phenomena that cannot easily be reproduced in laboratory. Laboratory investigations under controlled conditions can provide useful insights into how some of these failure modes develop and what the underlying mechanisms are.

Laboratory studies have underscored that the failure mode of a rock is intimately related to the porosity and its changes in response to an applied stress. On one hand, dilatancy is universally observed as a precursor to the inception of shear localization in the brittle faulting regime (Brace, 1978). On the other hand, plastic flow (associated with crystal plasticity and diffusive mass transfer) does not involve any volumetric change (Paterson and Wong, 2005). In the transitional regime of cataclastic flow (associated with homogeneously distributed microcracking), the scenario is more complicated since the pore space may dilate or compact in response to an applied stress field.

The transition from brittle faulting to plastic flow in compact carbonate rocks has been studied in detail, partly because it can readily be investigated in the laboratory without the use of elevated temperatures. Limestones and marbles, even the ones with very low porosity like the Carrara marble, undergo the brittle to plastic transition at room temperature for confining pressures accessible in the laboratory (Heard, 1960; Rutter, 1974). This is possibly because calcite requires relatively low shear stresses to initiate mechanical twinning and dislocation slip even at room temperature (Turner et al., 1954; Griggs et al., 1960). In Carrara marble, Fredrich et al. (1989) observed appreciable dilatancy while the compact marble undergoes cataclastic flow. In contrast, inelastic compaction was observed in association with cataclastic flow in limestone and chalk with porosities ranging from 3 to 45% (Baud et al., 2000; Vajdova et al., 2004).

Whereas the micromechanics of compaction and cataclastic flow in a porous siliciclastic rock such as sandstone have been studied extensively, not much is known about these processes in a porous limestone. The primary objective of this study is to characterize the damage evolution in deformed and failed samples of a porous micritic limestone, so as to gain insights into the micromechanics of brittle faulting and compactive cataclastic flow.

* Corresponding author Currently at: NOV Downhole, 500 Conroe Park West, Conroe, TX 77303, USA. Fax: +1 631 632 8240.
E-mail address: veronika@gmail.com (V. Vajdova).

0191-8141/$ – see front matter © 2010 Elsevier Ltd. All rights reserved.
doi:10.1016/j.jsg.2010.07.007

To investigate these two failure modes, two suites of triaxially compressed samples of Tavel limestone (with initial porosities in the range of 10–14%) were acquired at confining pressures of 30 and 150 MPa, respectively. To contrast with the failure under confinement, we conducted uniaxial compressive experiments on two samples. In addition we obtained a hydrostatically compacted sample for reference.

In parallel with this study, we also conducted a similar investigation of two allochemical limestones of higher porosities, which we intend to report in another publication. Microstructural observations described in these two studies motivated a development of a micromechanical model that treats a rock as a dual porosity medium, containing micropores and macropores. This model has been presented by Zhu et al. (2010). Here we use their findings to analyze the role of pores in Tavel limestone during both failure modes, brittle faulting and cataclastic flow.

2. Experimental procedure

2.1. Sample material and preparation

Tavel limestone is beige micritic limestone quarried in Tavel, France. Our blocks are considered to be similar to that studied previously by Vincké et al. (1998). The composition is dominated by calcite but a small amount of quartz (<10%) may be present. Tavel limestone is relatively homogeneous, with a small number of sparry grains (~11% of rock volume) embedded in a microcrystalline matrix with average grain size of ~5 μm. The sparry grains are usually elongate with an average equivalent diameter of ~25 μm. The elongate axes of the sparry grains seem not to have any preferred orientations.

In total we used ten deformed samples of Tavel limestone for microstructural observations. Two of these samples were previously deformed by Vajdova et al. (2004), and six additional samples from the same block were deformed for the present study. The initial porosity of these eight samples ranged between 9.5 and 11.4%, with an average value of 10.6%. We also deformed two samples (tu1 and th240) from a new block that has a higher porosity of ~13.5% (see Table 1 for list of samples). The porosity was calculated from the density of a dried sample assuming a solid composition of 100% calcite.

Cylindrical samples were cored perpendicular to the sedimentary bedding and ground to diameter of 18.4 mm and length of 38.1 mm. After it had been dried in vacuum at 80 °C for 48 h, each sample was first jacketed in a thin copper foil (of thickness 0.05 mm), and then polyolefine (heat-shrinkable) tubings were used to separate the rock from the confining medium (kerosene). Except for the two uniaxial compression tests (in which the axial strain was monitored solely by an externally mounted displacement transducer), two TML electric resistance strain gages (type FLA 10–11) were attached in orthogonal directions to the copper jacket to measure axial and transverse strains.

2.2. Mechanical deformation

The jacketed samples were deformed in the conventional triaxial configuration at room temperature using the same procedure as Vajdova et al. (2004). The triaxial compression experiments were performed at confining pressures of 30 and 150 MPa. Two samples were also deformed without any confinement. The confining pressure was measured with accuracy of 0.1 MPa, and during triaxial loading it was held constant to within 1%. The axial load was measured with an external load cell with an accuracy of 1 kN. To calculate the axial stress from the recorded axial load, the effect of bulging in a deformed sample was accounted for by evaluating the relative increase in cross-sectional area from the transverse strain. The displacement was measured outside the pressure vessel with a displacement transducer (DCDT) mounted between the moving piston and the fixed upper platen. With the knowledge of the stiffness of the loading frame (2.38×10^8 N/m) the axial displacement of the sample was obtained by subtracting the displacement of the loading frame from the apparent displacement recorded by the DCDT. The axial displacement was servo-controlled at a fixed rate (corresponding to a nominal strain rate of 1.3×10^{-5} s^{-1}).

The load, displacement, and strain gage signals were acquired by a 14-bit A/D converter at a sampling rate of 0.5 s^{-1} with resolutions of 0.3 MPa, 1 μm and 10^{-5}, respectively. Uncertainty in strain was estimated to be 2×10^{-4} (when calculated from the DCDT signal) and 10^{-5} (when measured directly by the strain gages). The volumetric strain was calculated using the relation $\epsilon_v = \epsilon_{||} + 2\epsilon_{\perp}$, where $\epsilon_{||}$ and $\epsilon_{\perp}$ are the axial and transverse strains, respectively. This formula neglects second-order contributions of strains to the volume change that may be appreciable at relatively large strain. While the transverse strains were generally small, the axial strains in some experiments exceeded 3%, and it is difficult to assess to what extent such strain gage data beyond 3% or so are reliable. For these cases we prefer to use the axial strain values as inferred from the DCDT data.

Acoustic emission (AE) activity was monitored via a piezoelectric transducer (PZT-7, 5 mm diameter, 1 MHz longitudinal resonant frequency) positioned on the flat surface of one of the end-plugs. However, it is typical of limestone deformation experiments that very little AE activity can be resolved, and accordingly the AE data were not of use in this study.

Table 1
Deformation history of samples studied.

Sample	Confining pressure [MPa]	Initial porosity [%]	Axial strain [%]	Total porosity reduction [%]	Comments	Reference
t0	0	–	0.0	0.0	Intact sample	This study
th240	240	13.4	1.2	1.0	Hydrostat (P^* = 180 MPa)	This study
tu1	0	13.5	0.6	–	Post-peak	This study
tu2	0	10.4	0.8	–	Post-peak	This study
tc1	150	10.7	0.6	0.9	Just beyond C^*	This study
tc2	150	11.4	2.2	2.0	Well beyond C^*	This study
tc3	150	10.4	6.8	<1.7	Just beyond $C^{*\prime}$	Vajdova et al., 2004
tb1	30	10.6	0.7	–	Pre-peak	This study
tb2	30	10.7	1.0	−0.1	Near-peak	This study
tb3	30	10.8	1.6	<0.1	Post-peak	This study
tb4	30	9.5	3.9	<−0.7	Post-peak, residual sliding	Vajdova et al., 2004

The samples were stressed to different stages of deformation and then unloaded. Upon retrieval from the apparatus they were encapsulated with epoxy and thin-sections were then cut along the central vertical plane of each sample. Thin-sections of a hydrostatically compacted sample and an intact sample were also prepared for reference.

2.3. Microstructural analysis

Microstructure of the intact and ten deformed samples was studied under optical microscope and scanning electron microscopes (SEM) on thin-sections. Optical microscopy was performed using a Nikon optical polarizing microscope. For SEM observations, the gold-coated thin-sections were studied using a LEO 1550 microscope with a voltage up to 10 kV. With the exception of Fig. 5b, all SEM micrographs presented here were acquired in the backscattered electron mode.

To quantify the stress-induced damage, we characterized the crack density in selected samples using a stereological technique. For each of these samples at least four SEM micrographs in randomly located areas on the thin-section were taken at 2500× magnification, covering a total area of at least 67,161 μm^2. An array of test lines spaced at 10 μm was then overlaid on each micrograph in a direction parallel or perpendicular to the maximum compression direction. The number of intercepts of microcracks with the test line was counted, and it was normalized by the test line length to give the linear intercept density (number of crack intersections per unit line length). The mean intercept densities for an array of test lines parallel and perpendicular to the maximum compression direction are denoted by $P_L^{\parallel}$ and $P_L^{\perp}$, respectively. These stereological parameters provide a quantitative measure of the crack density and its anisotropy (Underwood, 1970).

We also characterized the intensity of twinning on selected samples. For each of these samples, 20 optical micrographs were taken in randomly selected areas at 100× magnification, covering a total area of 33 mm^2. Due to the limited resolution only grains with diameter >10 μm were considered. We counted the number of twinned grains and normalized it by the investigated area to obtain a semi-quantitative parameter that we named the "twinning density".

3. Mechanical data

Table 1 summarizes the deformation history of all Tavel limestone samples used for the microstructural analysis. The convention is adopted that compressive stresses and compactive strains (i.e. shortening and porosity decrease) are positive. The maximum and minimum principal stresses will be denoted by σ_1 and σ_3, respectively. We summarize in Fig. 1 the mechanical data for the three suites of samples, in terms of the differential stress $\sigma_1 - \sigma_3$ as a function of axial strain.

In uniaxial compression samples tu1 and tu2 both failed by brittle faulting after undergoing strain softening and unstable stress drops (Fig. 1a). The peak stress for tu1 was significantly lower than tu2, probably due to its higher porosity (Table 1). Under a relatively low confining pressure of 30 MPa, the sample tb4 attained a peak stress significantly higher than the uniaxially compressed samples, after which strain softening occurred by a relatively stable stress drop to a residual level. The more porous sample tb3 attained a lower peak stress, and yet its post-peak behavior was more unstable (Fig. 1b). It is quite common in the brittle regime to have significant variability in the post-peak behavior from sample to sample (Paterson and Wong, 2005). Both samples failed by development of shear zones oriented at ~30° to σ_1. So that we can track the progressive development of damage at the same confining pressure, the other two samples (tb1 and tb2)

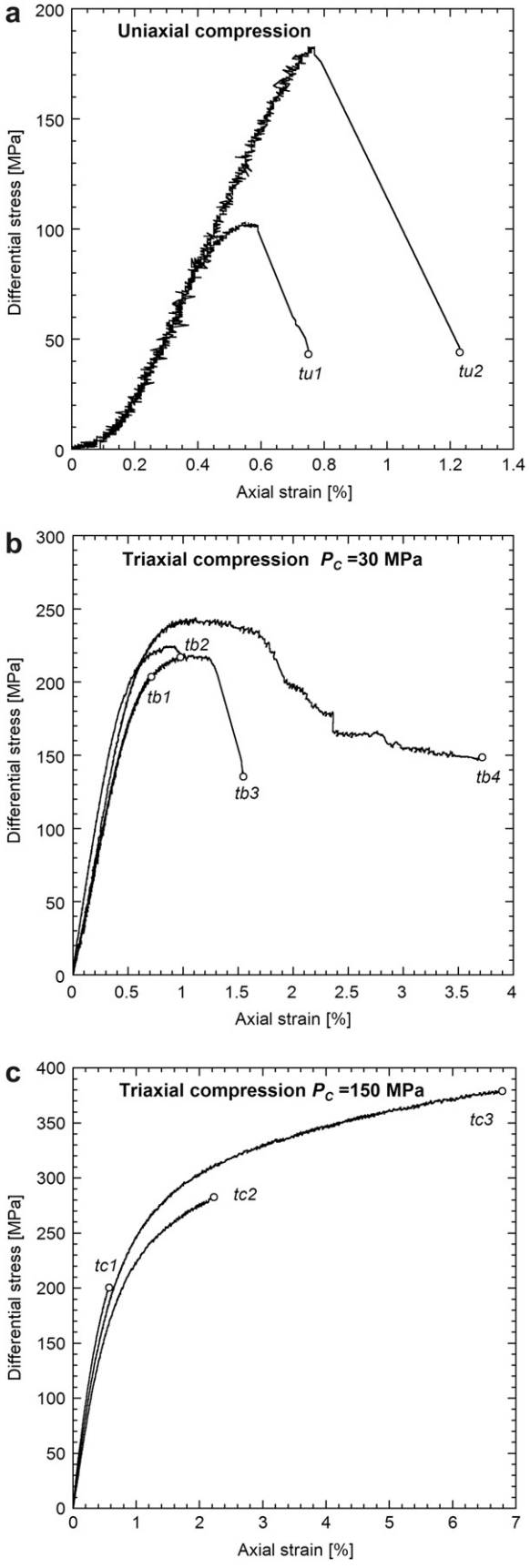

Fig. 1. Stress–strain curves of three suites of Tavel limestone samples. (a) Uniaxial compression tests on tu1 and tu2, with initial porosities 13.5 and 10.4%, respectively. Samples failed by brittle faulting. (b) Triaxial compression tests at confining pressure (P_c) of 30 MPa. The mechanical responses are typical of brittle faulting regime. (c) Triaxial compression experiments conducted at 150 MPa confining pressure. Strain hardening was observed. The samples underwent cataclastic flow.

were deformed to lower strains in the near-peak stage. Under a confining pressure of 150 MPa, the mechanical responses in the three tc-samples were similar in that they all showed strain hardening, with differential stress increasing monotonically with increasing strain (Fig. 1c). Strain localization was not observed in these samples that failed by cataclastic flow.

To illustrate the development of inelastic volume change, we show in Fig. 2 data for the mean stress $(\sigma_1 + 2\sigma_3)/3$ as a function of volumetric strain for the two series of samples deformed with confinement. For reference the data of Vajdova et al. (2004) for hydrostatic compression of a sample with 10.4% porosity is shown as the dashed curve, with the stress for the onset of pore collapse marked by P^*. As noted by Vajdova et al. (2004), in the cataclastic flow regime the volumetric strain evolves over three distinct stages with the progressive increase of differential stress (and mean stress). In the first stage, the triaxial compression curves basically coincided with the hydrostat up to a critical stress state (indicated by C^*). In the second stage at stress levels beyond C^*, there was an accelerated decrease in volume in comparison to the hydrostat, which implies that the deviatoric stress field provided significant inelastic contribution to the compactive strain. This phenomenon of "shear-enhanced compaction" persisted until the volumetric strain switched from compaction to a third stage of dilation. This transition from compactive to dilatant cataclastic flow occurred at the critical stress state (indicated by $C^{*\prime}$). It can be seen from Fig. 2 that while the sample tc1 was loaded to just beyond the onset of shear-enhanced compaction C^*, the sample tc2 was loaded to well beyond C^* and the sample tc3 to beyond the transition $C^{*\prime}$.

In contrast dilatancy was observed at a confining pressure of 30 MPa, in that the deviatoric stress field drove significant inelastic volume increase before the peak stress was attained. The stress at the onset of dilatancy is marked by C' in Fig. 2. The sample tb1 was loaded approximately to just beyond C'(in the absence of volumetric data due to transverse strain gage failure we have to rely on axial stress–strain curve). The sample tb2 was unloaded after significant dilatancy had developed in the peak stage. Samples tb3 and tb4 underwent large amount of dilatancy but the volumetric strain could not reliably be determined due to inhomogeneity in the post-peak deformation.

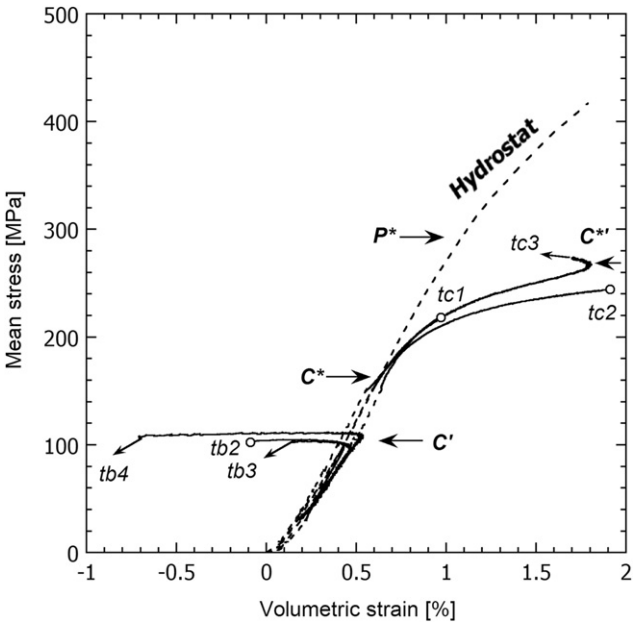

Fig. 2. Volumetric strain versus mean stress for triaxial compression of Tavel limestone. For reference, the hydrostatic data of Vajdova et al. (2004) are shown as the dashed line. Critical pressure for pore collapse is marked by P^*. C' indicates the onset of dilatancy in experiment at confining pressure 30 MPa, C^* and $C^{*\prime}$ indicate the onset of shear-enhanced compaction and the transition from compactive to dilatant cataclastic flow, respectively, in experiment at confining pressure 150 MPa. The small arrows indicate further deformation in samples tb3, tb4 and tc3 after volumetric strain data ceased to be reliable and were not plotted.

4. Microstructural observations

Observed under the optical microscope, the solid portion of Tavel limestone includes a number of sparry grains that are embedded in a microcrystalline matrix (Fig. 3a). Voids occur mostly as micropores within the microcrystalline matrix, and there is a small number of larger pores which can be resolved under an optical microscope only at higher magnifications. To analyze the spatial partitioning between micrite and sparite, we acquired four micrographs covering an area of ~0.25 mm^2 each at a magnification of 200× and manually traced out the sparry grain boundaries. Our analysis of these images of t0 indicates that the sparry grains (with diameters of ~10 μm or larger) represent ~11% of the volume of Tavel limestone.

Some of the macropores observed under an optical microscope are shown in Fig. 3b, where the boundary of a pore had been traced manually and its interior area darkened completely. The binarized image was analyzed using the ImageJ software a public domain image processing program developed at the National Institutes of Health. The area of each individual pore was determined, and the equivalent diameter of a circle with the same area was evaluated. Our analysis showed that these macropores in t0 contribute a relatively small porosity of 0.8% to the total (of ~11%), with equivalent diameters ranging from 3 to 30 μm (Fig. 3c). We should, however, note that in other Tavel limestone samples isolated pores with diameters up to 100 μm were observed. It is unavoidable that some grains would be plucked out when one prepares a thin-section for such a fine-grained rock, especially in the highly strained samples, but such instances were rare. Previous SEM observations have shown that the microporosity in a micritic limestone includes many submicron pores (Pittman, 1971; Anselmetti et al., 1998), and indeed the pore space in Tavel limestone is predominately made up of such micropores embedded in the micritic matrix (Fig. 4a).

4.1. Uniaxial compressive failure

The sample tu1 failed by the development of a through-going shear zone at ~30° with respect to σ_1. Fig. 4b shows an incipient shear zone (approximately connecting the two black arrows) we observed in the proximity of the through-going shear zone (white arrows). The inset shows a detail of the incipient shear zone where numerous stress-induced microcracks sub-parallel to σ_1 had emanated from the large as well as small pores. Some of these pore-emanated cracks have coalesced. The overall pattern of this incipient shear zone seems to be controlled by microcracking related to several macropores with diameters of ~15 μm lined up between the black arrows. This intensely damaged zone is contrasted with the relatively undamaged areas on its right.

4.2. Brittle faulting under confined compression

The sample tb1 was stressed to just beyond the onset of dilatancy (Fig. 1b). At high magnification under the SEM, microcracks were observed to have emanated from the macropores as well as micropores and propagated over relatively short distances (Fig. 4a). This is in contrast to sample tb2, which was stressed to just past the peak (Fig. 1b). Significant dilatancy was observed (Fig. 2), probably due to the propagation of numerous pore-emanated cracks aligned

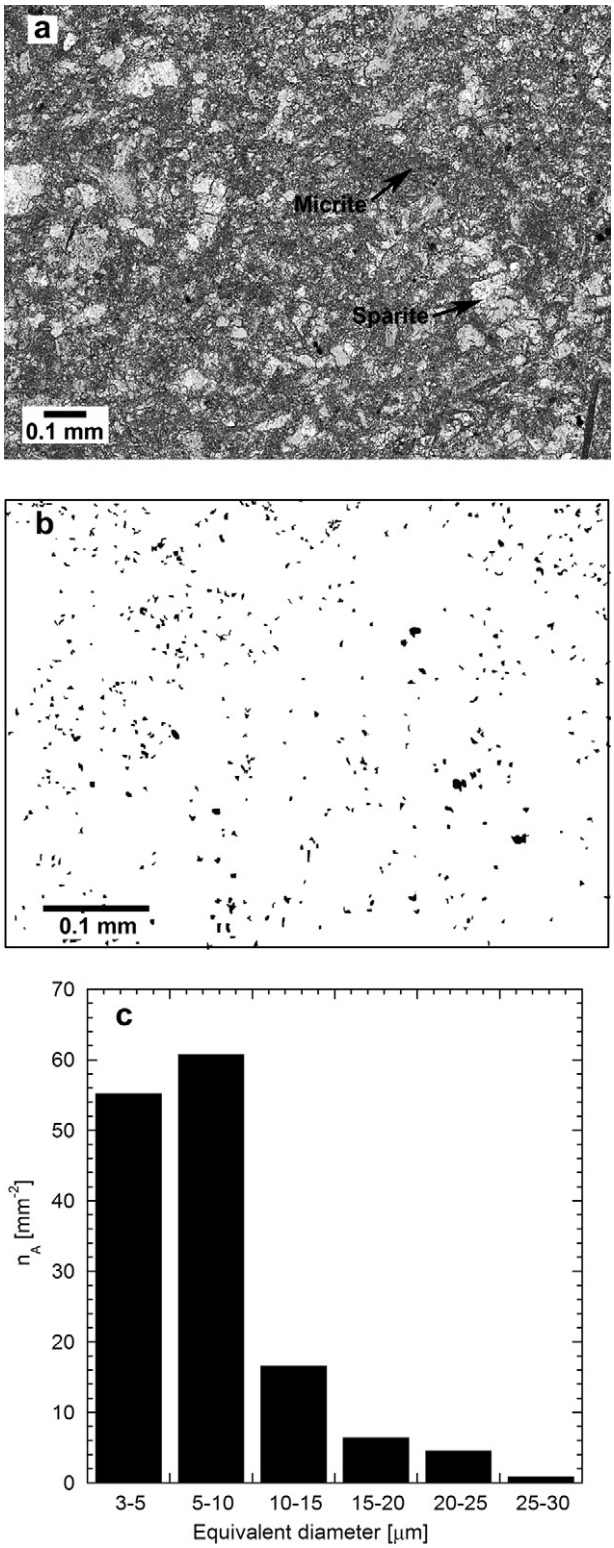

Fig. 3. (a) Optical micrograph of an intact Tavel limestone sample in transmitted light. Micrite and sparry grains are marked in the image. (b) Binarized image of intact Tavel limestone sample. Macropores resolved under optical microscope are shown in black. (c) Size distribution of pores in an undeformed Tavel limestone sample that can be resolved under optical microscope. The number of pores per unit area n_A is plotted versus equivalent diameter.

sub-parallel to σ_1, some of which had begun to coalesce (Fig. 4c). In one of the most intensely damaged zones (Fig. 4d) many microcracks have coalesced forming two major cracks converging on the large pore in the center of the micrograph. We also observed what appear to be wing cracks induced by stress concentrations near a sliding grain boundary (Fig. 4e).

Samples tb3 and tb4 were retrieved in the post-peak stage after significant stress drops. Intense microcracking and comminution were observed in the vicinity of shear zones that had developed in the failed samples (Fig. 4f).

4.3. Hydrostatic and shear-enhanced compaction under elevated pressure

Damage in the inelastically compacted samples is primarily associated with pore collapse. The sample th240 was hydrostatically compressed to an additional 60 MPa beyond the critical pressure P^*. Macropores at various stages of collapse were observed in this sample. We show in Fig. 5a a macropore which has a relatively circular cross-section with a diameter of ~20 μm, that is surrounded by a halo of cataclastic damage. A concentric rim of relatively intense damage has extended over a thickness of ~2 μm. While the spatial distribution of damage is circumferentially symmetric, its intensity decays with radial distance, such that the micritic matrix seems relatively undeformed beyond a thickness of ~6 μm. To gain a better perspective into the damage distribution around the pore surface, we tilted the sample slightly and observed the same area under the SEM in the secondary electron mode (Fig. 5b). The cavity is filled with what appear to be debris (from polishing the sample) mixed with epoxy, and the exposed pore surface is lined with a thin layer of microcracked materials.

The sample tc2 was loaded to well beyond the compactive yield stress C^* at a confining pressure of 150 MPa. Many of the macropores have collapsed in this sample. In contrast to the hydrostatically compacted sample, the spatial distribution of damage is asymmetric around the circumference, with the most intensive damage in two clusters that lie around the equator (Fig. 6a). The sample tc3 was unloaded after reaching well beyond the critical stress state $C^{*\prime}$. As illustrated in Fig. 6b, cataclastic pore collapse in this sample was not restricted to isolated macropores. The damage associated with a relatively elongate pore has extended over a very large distance. We also examined the incipient collapse of one of the largest macropores (Fig. 6c), showing numerous cracks that had emanated from micropores and propagated sub-parallel to σ_1. These pore-emanated cracks had begun to coalesce in a pattern akin to what we observed in samples in the tu- and tb-series which failed by shear localization, albeit on a small scale.

The inelastic compaction was accommodated by collapse of the spalled fragments into the void space, which would further perturb the surrounding stress field and induce microcracks to propagate to distances comparable to the pore dimension (Fig. 6d). The significant stress perturbation triggered by collapse of these pores had induced many such microcracks to propagate (Fig. 6e), which would cooperatively contribute to dilatancy in competition with the inelastic compaction from pore collapse. The transition $C^{*\prime}$ from compaction to dilatancy occurs when growth of dilatant microcracking becomes dominant.

4.4. Progressive development of microcracking and twinning

The intensity and spatial localization of damage in the form of microcracking are illustrated by our stereological data. Fig. 7a shows the linear intercept densities as function of axial strain we measured in the samples tb1, tb2 and tb4. There is an overall increase of crack density with deformation. In tb2 and tb4, the

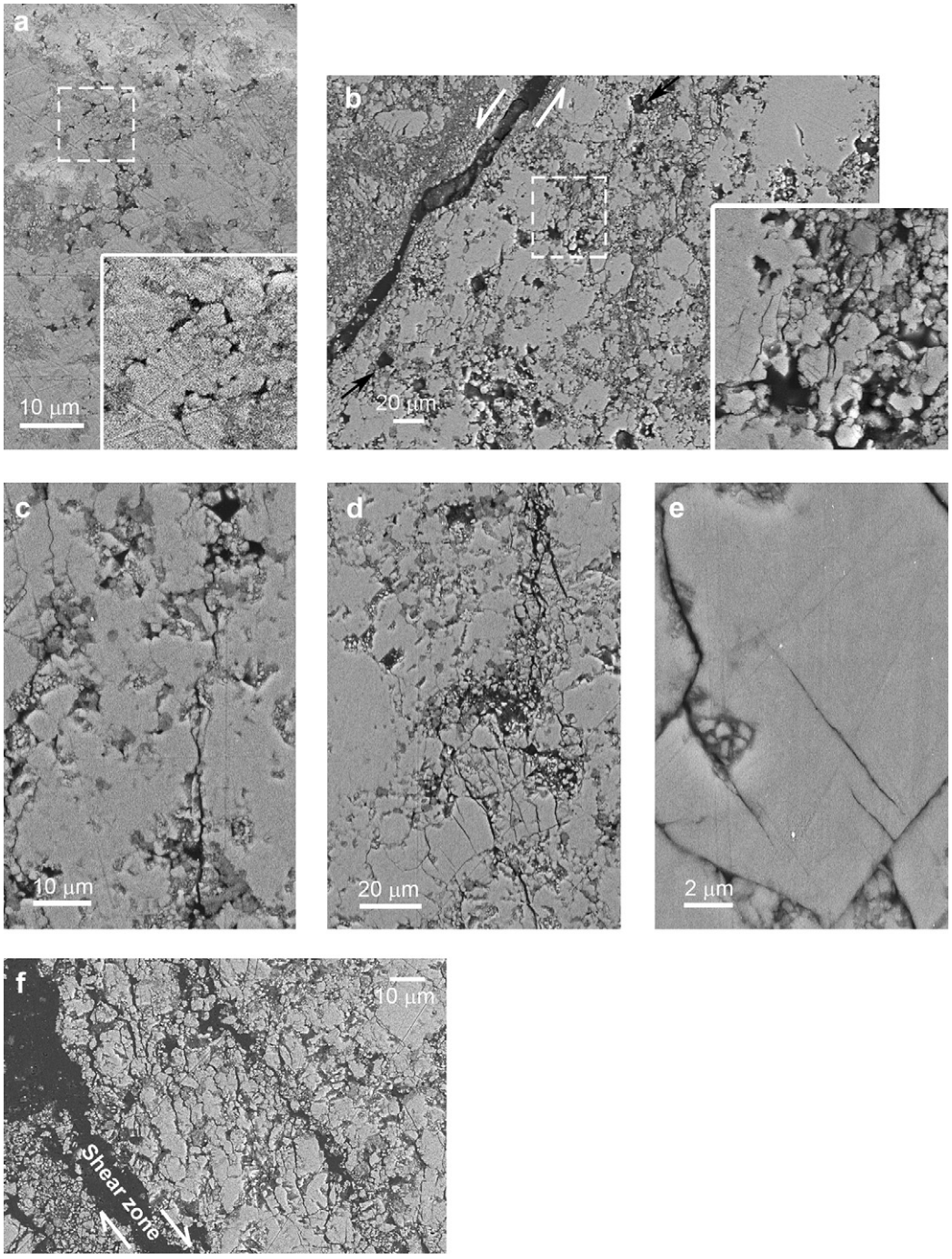

Fig. 4. Backscattered SEM images of samples failed by brittle faulting. Direction of σ_1 is vertical. (a) Sample tb1 stressed to just beyond the onset of dilatancy. Micropores in black are embedded in the micritic matrix. Inset shows a detail of framed area: short microcracks emanating from micropores. (b) Sample tu1 that failed in uniaxial compression. Inset shows a detail of framed area: an incipient shear zone (connecting two black arrows) developed in the proximity of the through-going shear zone (marked by white arrows). (c) Sample tb2 stressed to just beyond the peak. Propagation of pore-emanated cracks aligned sub-parallel to σ_1 was observed. (d) One of the most intensely damaged zones of sample tb2. Microcracks had coalesced and formed two major cracks converging on the large pore in the center of the micrograph. (e) In sample tb2, wing cracks nucleated by stress concentrations near the grain boundary were observed. (f) Sample tb3 stressed to the post-peak stage. Intense microcracking and comminution were observed in the vicinity of the shear zone.

density is anisotropic with $P_L^{\perp} > P_L^{\parallel}$, with the implication that the stress-induced microcracks are preferentially aligned along the σ_1 direction. In tb4, the development of shear localization is manifested by crack densities near the shear zone that are significantly higher than those at some distances away. In the cataclastic flow regime, there is also an increase of crack density with deformation from tc1 to tc3, but the density is relatively isotropic with $P_L^{\perp} \approx P_L^{\parallel}$ (Fig. 7b).

It should be emphasized that in addition to the pervasive cataclastic damage, our observations also indicate significant increase of twinning activity with deformation. In the brittle regime, a dramatic increase of twinning density was observed in the post-peak sample tb3, especially in areas near the shear zone (Fig. 7a). It should be noted that twining and microcracking are intertwined, in that the former can result in significant tensile stress concentration for the nucleation of microcracks (Olsson and Peng, 1976; Fredrich

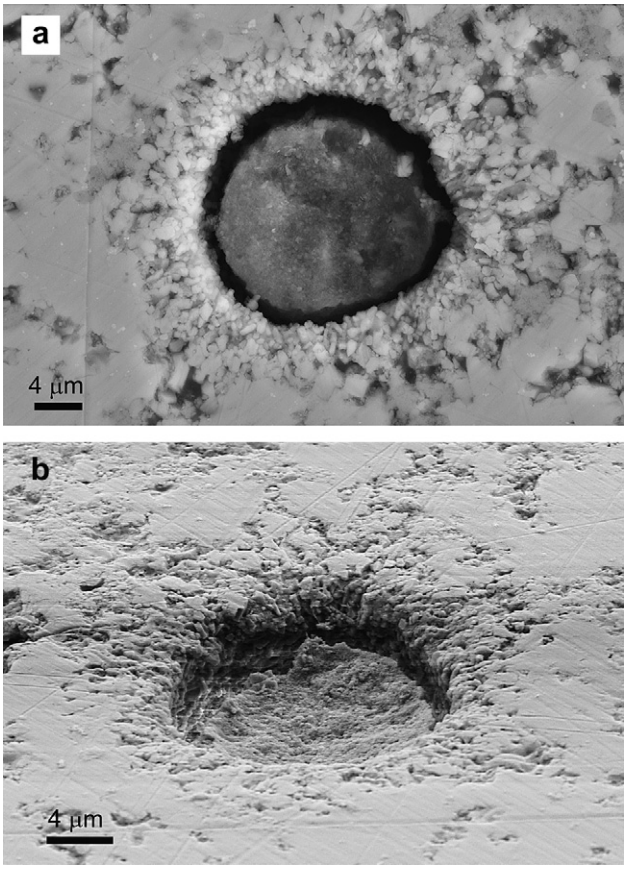

Fig. 5. (a) Backscattered SEM image of the hydrostatically compacted sample th240. A macropore surrounded by a halo of cataclastic damage was observed. The diameter of the macropore is ~20 μm, the concentric rim of particularly intense damage extended over a thickness of ~2 μm. (b) Secondary electron microscope image of the same macropore in (5a). The sample was rotated 90° anticlockwise and then tilted slightly. The cavity is filled with debris (from polishing the sample) mixed with epoxy, and the exposed pore surface is lined with a thin layer of microcracked materials.

et al., 1989). In the cataclastic flow regime, a progressive increase of twinning density with increasing strain was observed (Fig. 7b). As noted earlier, twinning in the sparry grains can be readily resolved under an optical microscope, and we have limited our observations to these grains corresponding to a relatively small portion (~11%) of the rock volume.

In their study of the use of calcite twinning for paleostress estimation, Rowe and Rutter (1990) considered three different measures of twinning activity and investigated comprehensively their dependences on grain size, stress, strain, strain rate and temperature. One of their measures is "twinning incidence", defined to be the percentage of grains in a given grain size class interval which contain optically visible twin lamellae. Since the equivalent diameters of the sparry grains in Tavel limestone span a relatively narrow range (from 10 to 50 μm), "twinning density" as defined here can be considered to be analogous to Rowe and Rutter's (1990) twinning incidence. They observed that this measure of twinning activity increases with grain size (at a constant level of differential stress) and linearly with stress (at a given grain size). Furthermore all three measures of twinning activity were observed to be independent of strain, strain rate and temperature. Since Rowe and Rutter (1990) focused on compact carbonate rocks, it requires further systematic investigation to assess the extent to which their conclusions on calcite twinning activity can be generalized to a limestone of significantly higher porosity. If indeed they also apply to Tavel limestone, then our data indicating an increase of twinning activity with increasing strain (Fig. 7) should be interpreted as due to the increase in differential stress that accompanied strain hardening in these samples.

5. Discussion

The development of dilatancy and micromechanics of brittle faulting in compact crystalline rocks and porous siliciclastic rocks have been extensively investigated (Paterson and Wong, 2005). Our observations here for the brittle faulting process in a porous limestone are similar in many respects. Shear localization does not develop until the post-failure stage after the peak stress has been attained. The post-peak deformation is stabilized by increasing pressure. Very high density of microcracking and pronounced stress-induced anisotropy is observed within the shear zones. However, there are two important differences. First, the pore space in Tavel limestone has numerous large and small pores, which assume a critical role in the nucleation of stress-induced microcracks. Second, cataclastic damage is often accompanied by crystal plasticity in the form of mechanical twinning, which may also contribute to dilatancy.

Inelastic compaction and cataclastic flow in porous carbonate rocks are qualitatively similar to siliciclastic rocks in many respects too (Vajdova et al., 2004). Notwithstanding these similarities in phenomenological behavior, our observations here show that the micromechanics can be very different. In a clastic rock such as sandstone, inelastic compaction derives primarily from grain crushing initiated by the stress concentrations at grain contacts (Menéndez et al., 1996; Wu et al., 2000). In contrast, inelastic compaction we observed in Tavel limestone is associated with cataclastic pore collapse, that seems to initiate from stress concentrations at the periphery of the relatively equant pores.

5.1. Pore-emanated cracking and unconfined compressive failure

In certain respects, our observations of pore-emanated cracking are captured by a fracture mechanics model formulated by Sammis and Ashby (1986) to analyze the micromechanics of brittle failure. The 2-dimensional model considers an elastic medium permeated by circular holes of uniform radius r (Fig. 8a). As the applied stress increases, a point is reached when the stress intensity factor of a small crack on the circular surface attains the critical value K_{IC}, at which point wing cracks would propagate to a distance ℓ parallel to the σ_1 direction (Fig. 8b). As the wing cracks propagate to longer distances, they interact with one another to induce an additional tensile stress intensity (Fig. 8c), ultimately leading to an instability with coalescence of the pore-emanated cracks.

Sammis and Ashby (1986) derived an expression for the maximum principal stress σ_1 as a function of the crack length ℓ, as well as the porosity Φ, the confining stress σ_3 and the fracture toughness (critical stress intensity factor) K_{IC}. A necessary condition for an instability (and stress drop) to develop is for $d\sigma_1/d\ell = 0$, when presumably the pore-emanated crack has propagated to a critical length for catastrophic crack coalesce to develop. For uniaxial compression (with $\sigma_3 = 0$), Zhu et al. (2010) have recently obtained an analytic estimate of the unconfined compressive strength σ_u that is in excellent agreement with numerical calculations based on Sammis and Ashby (1986) model. According to this analytic approximation, the unconfined strength decreases with increasing porosity and average pore radius:

$$\sigma_u = \frac{1.325}{\Phi^{0.414}} \frac{K_{IC}}{\sqrt{\pi r}} \quad (1)$$

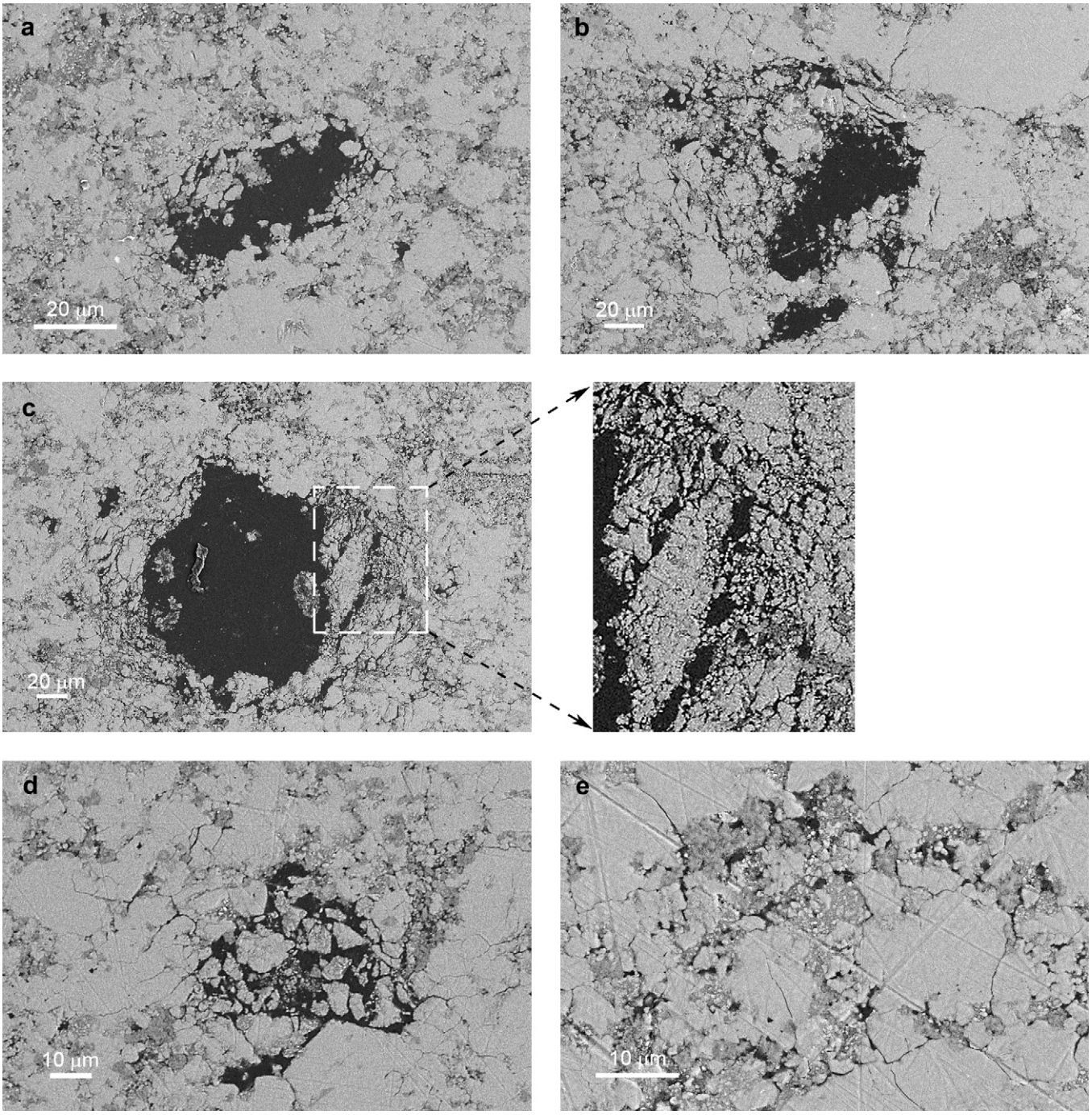

Fig. 6. Backscattered SEM images of samples failed by cataclastic flow. Direction of σ_1 is vertical. (a) The sample tc2 was stressed to well beyond the compactive yield stress C^*. The spatial distribution of damage is asymmetric around the circumference of the macropore. (b) Sample tc3 was loaded to just beyond C^*. A relatively elongated pore with cataclastic damage that had extended over a very large distance was observed. (c) One of the largest collapsed macropores of sample tc3. Numerous pore-emanated cracks propagated sub-parallel to σ_1. Intensive cataclastic damage around the equator was observed, with details inside the dashed rectangle shown in the zoomed-in figure on the right. (d) Collapse of spalled fragments into a macropore in sample tc3. Stress-induced microcracks propagated to distances comparable to the pore dimension. (e) Intensive stress-induced microcracks propagated to long distance in sample tc3.

Zhu et al. (2010) compiled laboratory data for the unconfined compressive strength of micritic and allochemical limestones (made up of 80% or more calcite) with porosities ranging up to 30%, and compared them with this analytic approximation of the Sammis and Ashby (1986) model (Fig. 9). They observed that the data seem to fall into two groups: those for compact micritic limestones (with porosity <15%) can be bracketed by the two theoretical curves for $K_{IC}/\sqrt{\pi r} = 35$ and 75 MPa, whereas those for allochemical and porous micritic limestones can be bracketed by the two theoretical curves for $K_{IC}/\sqrt{\pi r} = 5$ and 22 MPa. As expected, our Tavel limestone data fall within the compact micritic group, corresponding to $K_{IC}/\sqrt{\pi r} = 35$ and 54 MPa, respectively. If we assume a K_{IC} value of 0.2 MPa $m^{1/2}$ based on fracture mechanics measurements on calcite (Atkinson and Meredith, 1987), then the pore-emanated cracking model together with the unconfined strength data imply that the Tavel limestone samples tu1 and tu2

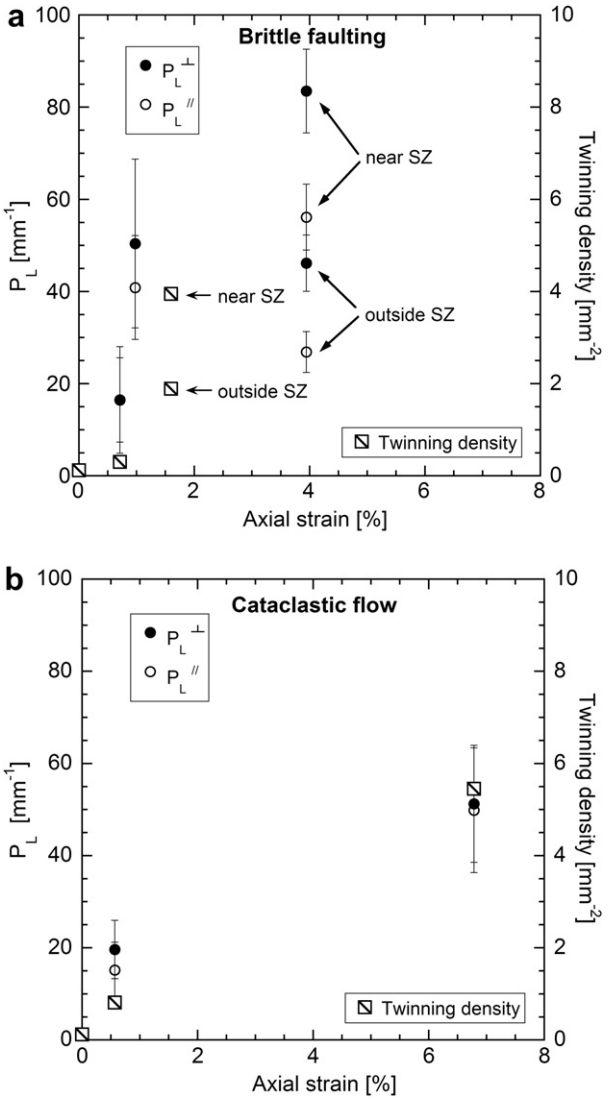

Fig. 7. Linear intercept densities (P_L) and twinning densities as functions of axial strain for samples failed in (a) brittle regime (tb1, tb2, tb3 and tb4), and (b) cataclastic flow regime (tc1 and tc3). Arithmetic mean values of the linear intercept densities in parallel and vertical directions are denoted by solid and open circles, respectively. Error bars correspond to standard deviations. Twinning density is represented by the square symbol. SZ refers to shear zone.

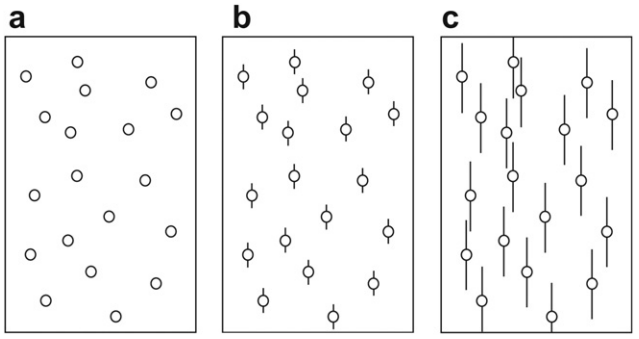

Fig. 8. Sammis and Ashby's (1986) pore-emanated cracking model. (a) A 2-dimensional elastic medium is permeated by circular holes of uniform radius *r*. (b) Cracks emanate from circular pores when subjected to a remotely applied axial stress. (c) Propagation of pore-emanated cracks will lead to their coalescence and consequently to instability and macroscopic failure.

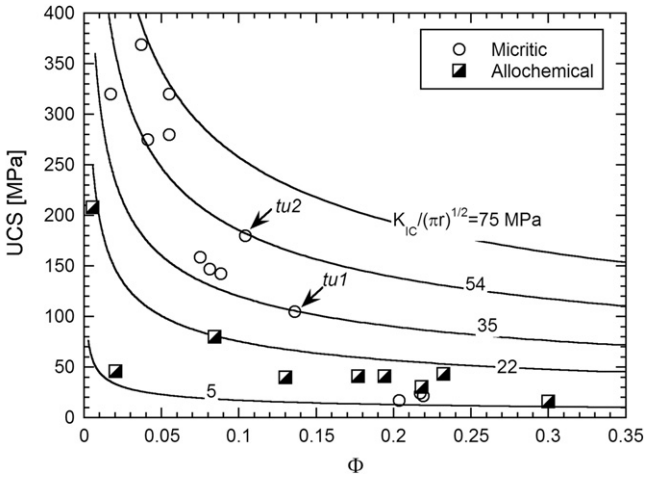

Fig. 9. Comparison of theoretical predictions of Sammis and Ashby (1986) model with laboratory data on unconfined compressive strength (UCS) of micritic and allochemical limestones. Theoretical curves of UCS as function of porosity for five different values of $K_{IC}/\sqrt{\pi r}$ are plotted. Experimental data of micritic and allochemical limestones compiled by Zhu et al. (2010) are shown as circles and squares, respectively. Uniaxial experiment data of tu1 and tu2 fall on the two theoretical curves for $K_{IC}/\sqrt{\pi r}$ = 35 and 54 MPa, respectively.

have average pore diameters of $2r$ = 20 and 8 μm, respectively. These estimates are comparable to our data for the macropore sizes (Fig. 3c), and can be considered to be in agreement with our SEM observations which indicate that the coalescence often involves cracks that emanated from such macropores.

5.2. Development of dilatancy and brittle faulting under confinement

Although Sammis and Ashby's (1986) pore-emanated cracking model captures many aspects of the failure process under unconfined compression, its application to compressive failure under

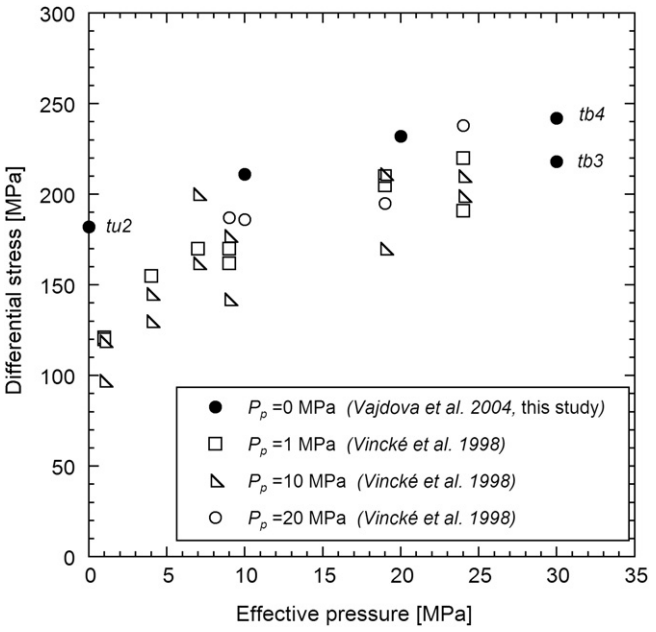

Fig. 10. Compilation of peak stress data in the brittle faulting regime for nominally dry and oil-saturated samples of Tavel limestone. There is an overall trend for the nominally dry samples to be somewhat stronger.

confinement is questionable. As noted by Wong (1990), this model predicts that confinement can inhibit localization of brittle failure at a lateral stress level that is significantly lower than experimental observations for most porous rocks. Assuming parameter values inferred from the above analysis of unconfined compressive failure ($K_{IC}/\sqrt{\pi r}$ = 35 or 54 MPa, and Φ = 13.5 or 10.4%), it can be shown that Sammis and Ashby's (1986) model predicts that pore-emanated cracking and coalescence would be inhibited at a confining pressure as low as 1 MPa, in discrepancy with laboratory data which show that brittle faulting in Tavel limestone persists up to a confining pressure of 30 MPa (Vajdova et al., 2004).

We compile in Fig. 10 peak stress data for nominally dry and saturated samples of Tavel limestone that fail by brittle faulting. The dry data include those for tu2, tb3 and tb4 in this study, as well as others of Vajdova et al. (2004). For comparison we show the data of Vincké et al. (1998) for samples of Tavel limestone deformed under drained condition at three different pore pressures P_p. A mineral oil was used to saturate these samples (E. Bemer, private communication, 2009). We have not included the data point for tu1 since it was cored from a block more porous than either the block of Vajdova et al. (2004) or Vincké et al. (1998).

Brittle faulting was observed at effective pressure ($\sigma_3 - P_p$) up to 30 MPa, and there is an overall trend for the dry samples to be somewhat stronger than the saturated counterparts. The peak stress as a function of effective pressure follows an approximately linear trend. A micromechanical model for brittle failure that predicts such a linear pressure dependence is the sliding wing crack model (Horii and Nemat-Nasser, 1986; Ashby and Sammis, 1990; Kemeny and Cook, 1991). This prompted Vajdova et al. (2004) to analyze their brittle failure data using Ashby and Sammis' (1990) 2-dimensional wing crack model. The applied far-field stresses induce a shear traction across the faces of a pre-existing crack (of length $2a$), and if the resolved shear traction exceeds the frictional resistance on the closed crack surface, frictional slip occurs which also induces tensile stress concentrations at the two tips that may nucleate and propagate wing cracks. The driving force is characterized by the stress intensity factor at the tip of the putative wing crack, which will attain the critical value K_{IC} with increased loading, at which point the wing crack nucleates and propagates along a curved path to ultimately reach a stable orientation parallel to the direction of σ_1. As the wing cracks propagate to longer distances, they interact and ultimately coalesce to result in an instability.

Using the sliding wing crack model to fit their Tavel limestone data, Vajdova et al. (2004) inferred a friction coefficient 0.34, initial damage (which characterizes the density of sliding cracks and their length) D_o = 0.28 and normalized fracture toughness $K_{IC}/\sqrt{\pi a}$ = 77 MPa. Although we did observe a few examples of what appear to be sliding wing cracks (Fig. 4e), it is unlikely that they were sufficiently numerous to give the relatively high D_o value inferred by Vajdova et al. (2004). Nemat-Nasser (1985) has argued that since the growth behavior of a sliding wing crack is qualitatively similar to that induced by tensile stress concentrations arising from other mechanisms (such as elastic mismatch between neighboring grains, stress perturbation due to twinning or dislocation slip, and equant voids), it provides a useful mathematical analogue for analyzing the propagation and coalescence of a multiplicity of stress-induced cracks in a brittle rock. In this context, it is of interest to note that the fracture toughness values ($K_{IC}/\sqrt{\pi r}$ = 54 MPa and $K_{IC}/\sqrt{\pi a}$ = 77 MPa) inferred from the pore-emanated cracking and sliding wing crack models are comparable, even though very different defects (pre-existing pores of radius r and sliding cracks of half-length a) are invoked in these models. This suggests an interpretation of the parameter D_o as a generic measure of the density and dimension of hybrid defects in our limestone, that may include pre-existing macropores and micropores, sparry grain boundaries and deformation twins. While microcracking emanating from an isolated pore is readily arrested by the application of a relatively small lateral stress, the additional tensile stress concentrations induced by neighboring pores, sliding cracks and twinning may cooperatively promote the further propagation of pore-emanated microcracks and ultimately their coalescence.

5.3. Inelastic compaction and cataclastic pore collapse

Our observations show that even though pore collapse in siliciclastic and carbonate rocks both involve distributed microcracking, the spatial patterns of cataclastic damage are significantly different, probably a manifestation of fundamentally different micromechanical processes. In a sandstone hydrostatically compacted to beyond P^*, numerous intragranular microcracks would nucleate and radiate from grain contacts. Indeed such microstructural observations have motivated Zhang et al. (1990) to formulate a Hertzian fracture mechanics model which predicts that the compactive yield stress of porous sandstone would scale inversely with porosity and grain size, in basic agreement with experimental observations in siliciclastic rocks (Wong et al., 1997). In contrast, our observations show that when Tavel limestone was hydrostatically stressed to beyond the critical pressure P^*, a halo of cataclastic damage would develop symmetrically around the circumference of a macropore (Fig. 5).

Under a remotely applied hydrostatic stress, the maximum compressive stress in the vicinity of a macropore is given by the "hoop stress" on the surface of the central pore, while the boundary condition constrains the radial stress to vanish on the surface. If the pore geometry can be approximated as spherical, then the symmetry constrains the stress field to be uniform on the surface, and accordingly when the limestone is stressed to beyond P^*, yielding would occur and damage is predicted to develop symmetrically around the macropore akin to what we observed in sample th240 (Fig. 5). Laboratory data indicate an overall trend for the pore collapse pressure to decrease with increasing porosity (Vajdova et al., 2004).

Under nonhydrostatic loading, the local stress field in the vicinity of a pore is more complicated. Consider a remote stress field $S_1 > S_2 = S_3$ corresponding to a conventional triaxial compression test in the laboratory (Fig. 11a). With reference to a cylindrical coordinate system (ρ, θ, z), the maximum compressive stresses associated with a spherical pore are located along the equator of the central sphere (at $z = 0$ and $\rho = r$), with the axial

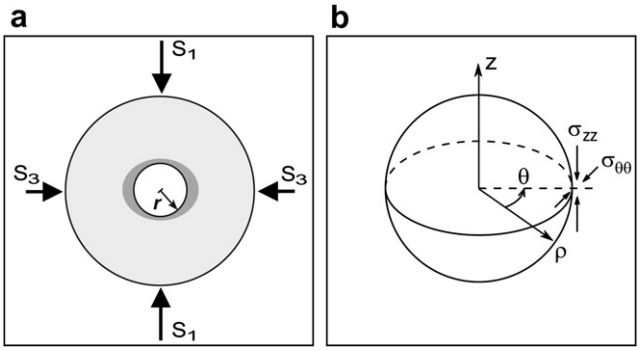

Fig. 11. (a) Schematic diagram of damage (dark gray) distribution on the periphery of a macropore (white circle) at the onset of pore collapse induced by remotely applied principal stresses S_1 and S_3. (b) Local stress field at the vicinity of the macropore. The local principal stresses σ_{zz} and $\sigma_{\theta\theta}$ act along the axial and azimuthal directions, respectively. Due to the boundary condition, the radial stress (not shown) is zero.

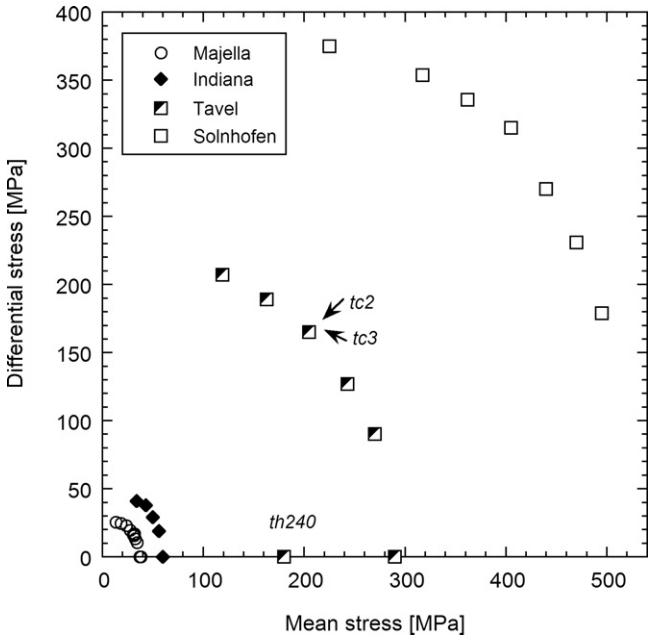

Fig. 12. Compactive yield caps for onset of shear-enhanced compaction shown in the stress space for four limestones with porosities ranging from 3 to 30%. The critical stress (C^*) data of samples tc2, tc3 and th240 are also indicated. There is an overall trend for the cap to expand with decreasing porosity.

stress σ_{zz} and azimuthal stress $\sigma_{\theta\theta}$, corresponding to the maximum and intermediate principal stresses (Fig. 11b). The boundary condition constrains the radial stress $\sigma_{\rho\rho}$ to be zero, representing the minimum principal stress. When the limestone is stressed to beyond C^*, yielding would occur and damage is predicted to first develop around the equator (Fig. 11a), similar to the patterns observed in samples tc2 and tc3 (Fig. 6a–d).

In Fig. 12 the compactive yield stress C^* of samples tc2 and tc3 are compared with laboratory data obtained by Baud et al. (2000, 2009) and Vajdova et al. (2004) for four limestones with porosities ranging from 3 to 30%. The C^* data map out compactive yield caps that are approximately elliptical in shape, with major and minor axes that expand with decreasing porosity. A micromechanical model that can capture aspects of this failure process is the plastic pore collapse model (e.g., Curran and Carroll, 1979). For Solnhofen limestone (with 3% porosity), Baud et al. (2000) observed that its yield cap can be interpreted using such a model, with pore collapse induced by crystal plasticity processes such as dislocation slip and deformation twinning. Our microstructural observations in the more porous Tavel limestone indicate at least two major discrepancies with this plastic pore collapse model. First, pore collapse typically initiates at the larger pores, while the plastic pore collapse model predicts that it is equally likely for collapse to initiate from a large or a small pore. Second, cataclasis and microcracking (rather than crystal plasticity) seem to be the dominant deformation mechanisms in the proximity of a pore that has collapsed.

To circumvent these limitations of a plastic pore collapse model, Zhu et al. (2010) recently developed a micromechanical model that can capture many aspects of cataclastic pore collapse we reported here. Motivated by microstructural observations, the pore size distribution of a limestone was treated as bimodal, with the total porosity partitioned between the macroporosity and microporosity. Hence the limestone represents a dual porosity medium, that yields first at the large pores, each of which is surrounded by an effective medium containing numerous micropores. Cataclastic yielding (in the form of unconfined brittle failure) of this effective medium obeys the Mohr-Coulomb or Drucker-Prager criterion, with failure parameters that are dependent on the porosity and pore size. According to this model, the compactive yield stress data of Tavel limestone imply that the micropores have an average diameter of $\sim$1 μm, comparable to our SEM observations (Fig. 4a).

While the dual porosity model of Zhu et al. (2010) captures a number of micromechanical processes which cannot be described in a plastic pore collapse model that assumes a single type of porosity, the introduction of microporosity as a distinct entity embedded in the effective medium implies that predictions of the model hinge on geometric and mechanical attributes of the micropores which are difficult to quantify. This is an important issue that warrants further investigation. It would also be useful to develop a micromechanical model for evolution of the yield cap with porosity change. Since our observations indicate that crystal plasticity mechanisms (twinning and possibly dislocation slip) would be operative to a certain extent, their contributions to inelastic compaction should be appropriately incorporated in such a model.

5.4. Microcrack density: comparison with other rocks

Our stereological data are qualitatively similar to those for a compact crystalline rock such as granite and gabbro deformed in the brittle faulting regime (Wong, 1985) and sandstones in both the brittle faulting and cataclastic flow regimes (Menéndez et al., 1996; Wu et al., 2000). However, the intercept density values we measured for Tavel limestone (Fig. 7) are almost 1 order of magnitude higher than these earlier data which are typically on the order of 1 mm^{-1}. For brittle faulting regime the granite, gabbro and sandstone samples (all deformed at strain rate 10^{-5} s^{-1}) were loaded in pre-failure stage to 90–95% of peak stress resulting in $P_L^{\parallel}$ values 5.71, 1.2–2.3 and 2.9 mm^{-1}, respectively. (The range of values for gabbro reflects the effect of confining pressure between 100 and 350 MPa) In comparison, the linear intercept density $P_L^{\parallel}$ for Tavel limestone at 80% of peak stress is 17 mm^{-1}. For cataclastic flow regime in Berea sandstone the $P_L^{\parallel}$ value is 1.7 mm^{-1} at stress level just before C^*, compared to 15 mm^{-1} for Tavel limestone at C^*. This data indicate that Tavel limestone can accommodate much higher microcrack density before a failure occurs.

This difference arises possibly because the average grain size in our micritic limestone is 1–2 orders of magnitude finer than the granite, gabbro and sandstone previously investigated. It was noted by Wong (1985) that if d denotes the average grain size, then the non-dimensional parameter $P_L d$ would provide a more appropriate measure of the crack density for comparison between different rocks.

6. Conclusion

In this study, the evolution of microstructural damage was described for the compressive failure of porous micritic limestone deformed in the laboratory. The microstructural observations in conjunction with micromechanical modeling identified porosity and the dominantly micritic texture of the rock as two major features affecting micromechanics of brittle faulting and cataclastic flow. Both failure modes are associated primarily with cataclastic damage although mechanical twinning was present too. The microcracks initiate as pore-emanated cracks from micropores and macropores alike but macropores seem to drive the crack propagation, which eventually leads to crack coalescence in brittle faulting or pore collapse in compactive cataclastic flow.

In brittle faulting, microcracks are oriented parallel to σ_1 and their length increases with loading approaching the peak stress. Localization is caused by coalescence of cracks running parallel to σ_1. Besides the microstructural observations, the importance of macropores in crack coalescence for uniaxial compression is

implied also by Sammis and Ashby's (1986) model. In case of brittle faulting under confined conditions, additional stress concentration mechanisms are likely to be present, assisting the microcrack growth (such as elastic mismatch between grains, sliding cracks or twinning) and ultimately leading to crack coalescence and localization. Quantitative observations indicate that the crack orientation anisotropy becomes obvious only beyond the peak stress. The intensity of deformation (cracks and twinning density) decreases with distance from the shear zone.

In compactive cataclastic flow the pore-emanated microcracks do not show any preferred orientation but allow fragmentation of the matrix that can consequently collapse into the macropores. The stress perturbation resulting from the pore collapse promotes the opening of additional microcracks. The interplay of compaction and dilatancy leads to the transitional state $C^{*\prime}$ as dilatancy overcomes compaction at high strain. At that stage, crack coalescence in a pattern similar to brittle samples was observed and the crack density was comparable to that of a brittle sample at peak stress, when a shear zone begins to develop. Hydrostatic compaction is characterized by the development of a symmetric halo of cataclastic damage around a circular pore while the damage is asymmetric in case of shear-enhanced compaction, in agreement with the idea that macropores represent the dominant stress concentrators.

Acknowledgments

We are grateful to Elizabeth Bemer and Patrick Baud who kindly provided the blocks of Tavel limestone. We want to thank Patrick Baud for help with experiments, Jim Quinn for assistance with SEM microscopy and Wenlu Zhu for discussions on microstructure interpretation. We also want to thank Ernie Rutter and an anonymous reviewer for their valuable comments and suggestions. This research was partially supported by the Office of Basic Energy Sciences, Department of Energy under grants DE-FG02-99ER14996 and DE-SC0004118.

Appendix. Supporting material

Supplementary material associated with this article can be found, in the online version at doi:10.1016/j.jsg.2010.07.007.

References

Anselmetti, F.S., Luthi, S., Eberli, G.P., 1998. Quantitative characterization of carbonate pore systems by digital image analysis. AAPG Bull. 82, 1815–1836.
Ashby, M.F., Sammis, C.G., 1990. The damage mechanics of brittle solids in compression. Pure Appl. Geophys. 133, 489–521.
Atkinson, B.K., Meredith, P.G., 1987. Experimental fracture mechanics data for rocks and minerals. In: Atkinson, B.K. (Ed.), Fracture Mechanics of Rock. Academic Press, London, pp. 477–525.
Baud, P., Schubnel, A., Wong, T.-f, 2000. Dilatancy, compaction and failure mode in Solnhofen limestone. J. Geophys. Res. 195, 19289–19303.
Baud, P., Vinciguerra, S., David, C., Cavallo, A., Walker, E., Reuschle, T., 2009. Compaction and failure in high porosity carbonates: mechanical data and microstructural observations. Pure Appl. Geophys 166, 869–898.
Brace, W.F., 1978. Volume changes during fracture and frictional sliding: a review. PAGEOGH 116, 603–614.
Curran, J.H., Carroll, M.M., 1979. Shear stress enhancement of void compaction. J. Geophys. Res. 84, 1105–1112.
Fredrich, J.T., Evans, B., Wong, T.-f, 1989. Micromechanics of the brittle to plastic transition in Carrara marble. J. Geophys. Res. 94, 4129–4145.
Griggs, D.T., Turner, F.J., Heard, H.C., 1960. Deformation of rocks at 500° to 800°C. In: Griggs, D., Handin, J. (Eds.), Rock Deformation. Memoir. Geological Society of America, vol. 79, pp. 39–104.
Heard, H.C., 1960. Transition from brittle fracture to ductile flow in Solnhofen limestone as a function of temperature, confining pressure and interstitial fluid pressure. In: Griggs, D., Handin, J. (Eds.), Rock Deformation. Memoir. Geological Society of America, vol. 79, pp. 193–226.
Horii, H., Nemat-Nasser, S., 1986. Brittle failure in compression: splitting, faulting and brittle-ductile transition. Phil. Trans. R. Soc. Lond. 319, 337–374.
Kemeny, J.M., Cook, N.G.W., 1991. Micromechanics of deformation in rocks. In: Shah, S.P. (Ed.), Toughening Mechanisms in Quasi-Brittle Materials. Kluwer Acad., Norwell, Mass, pp. 155–188.
Menéndez, B., Zhu, W., Wong, T.-f, 1996. Micromechanics of brittle faulting and cataclastic flow in Berea sandstone. J. Struct. Geol. 18, 1–16.
Nemat-Nasser, S., 1985. Discussion of geometric probability approach to the characterization and analysis of microcracking in rocks. Mech. Mater. 4, 277–281.
Olsson, W.A., Peng, S.S., 1976. Microcrack nucleation in marble. Int. J. Rock Mech. Min. Sci. 13, 53–59.
Paterson, M.S., Wong, T-f, 2005. Experimental Rock Deformation – The Brittle Field, second ed. Spinger-Verlag, New York.
Pittman, E.D., 1971. Microporosity in carbonate rocks. AAPG Bull. 55, 1873–1878.
Rowe, K.J., Rutter, E.H., 1990. Paleostress estimation using calcite twinning: experimental calibration and application to nature. J. Struct. Geol. 12, 1–17.
Rutter, E.H., 1974. The influence of temperature, strain rate and interstitial water in the experimental deformation of calcitic rocks. Tectonophysics 22, 311–334.
Sammis, C.G., Ashby, M.F., 1986. The failure of brittle porous solids under compressive stress states. Acta Metall. 34, 511–526.
Turner, F.J., Griggs, D.T., Heard, H.C., 1954. Experimental deformation of calcite crystals. Geol. Soc. Am. Bull. 65, 883–954.
Underwood, E.E., 1970. Quantitative Stereology. Addison Wesley, Reading.
Vajdova, V., Baud, P., Wong, T.-f, 2004. Compaction, dilatancy and failure in porous carbonate rocks. J. Geophys. Res. 109, B05204. doi:10.1029/2003JB002508.
Vincké, O., Boutéca, M.J., Piau, J.M., Fourmaintraux, D., 1998. Study of the effective stress at failure. In: Thimus, J.-F., Abousleiman, Y., Cheng, A.H.-D., Coussy, O., Detournay, E. (Eds.), Poromechanics, a Tribute to Maurice A. Biot. A.A. Balkema, Rotterdam, pp. 635–639.
Wong, T.-f., 1985. Geometric probability approach to the characterization and analysis of microcracking in rocks. Mech. Mater. 4, 261–276.
Wong, T.-f., 1990. Mechanical compaction and the brittle-ductile transition in porous sandstones. In: Knipe, R.J., Rutter, R.H. (Eds.), Deformation Mechanisms, Rheology and Tectonics. Geol. Society Special Publication, vol. 54, pp. 111–122. London.
Wong, T.-f., David, C., Zhu, W., 1997. The transition from brittle faulting to cataclastic flow in porous sandstones: mechanical deformation. J. Geophys. Res. 102, 3009–3025.
Wu, X.Y., Baud, P., Wong, T.-f, 2000. Micromechanics of compressive failure and spatial evolution of anisotropic damage in Darley Dale sandstone. Int. J. Rock Mech. Min. Sci. 37, 143–160.
Zhang, J., Wong, T.-f., Davis, D.M., 1990. Micromechanics of pressure-induced grain crushing in porous rocks. J. Geophys. Res. 95, 341–352.
Zhu, W., Baud, P., Wong, T.-f, 2010. Micromechanics of cataclastic pore collapse in limestone. J. Geophys. Res. 115, B04405, doi:10.1029/2009JB006610.